Science Advances
AAAS

Supplementary Materials for

A tandem radiative/evaporative cooler for weather-insensitive and high-performance daytime passive cooling

Jinlei Li *et al.*

Corresponding author: Bin Zhu, binzhu@nju.edu.cn; Shanhui Fan, shanhui@stanford.edu; Jia Zhu, jiazhu@nju.edu.cn

Sci. Adv. **8**, eabq0411 (2022)
DOI: 10.1126/sciadv.abq0411

This PDF file includes:

Supplementary Text

Supplementary Text 1. Theoretical cooling power

The radiative cooling power is determined by (*18, 20, 21, 28, 46*).

$$P_{\mathrm{R}} = \left(P_{\mathrm{rad}} - P_{\mathrm{amb}}\right) - P_{\mathrm{sun}} - P_{\mathrm{conv+cond}} \quad \text{(S1)}$$

in which, P_{rad} and P_{amb} denote radiative power from a cooler and absorbed ambient radiative power on the cooler, respectively. P_{sun} is the power of absorbed sunlight. $P_{\mathrm{conv+cond}}$ is the loss of cooling power due to convection and conduction.

In Equation S1, the radiative power from a cooler is:

$$P_{\mathrm{rad}} = \sigma \varepsilon_{\mathrm{c}} T_{\mathrm{c}}^4 \quad \text{(S2)}$$

where σ is the Stefan-Boltzmann constant, ε_{c} is the mid-infrared emissivity of the cooler, and T_{c} is the temperature of the cooler.

$$P_{\mathrm{amb}} = \alpha_c \sigma \varepsilon_{\mathrm{amb}} T_{\mathrm{amb}}^4 \quad \text{(S3)}$$

in which, α_c, $\varepsilon_{\mathrm{amb}}$, and T_{amb} represent the mid-infrared absorptivity of the cooler, mid-infrared emissivity and temperature of the ambient, respectively. According to Kirchhoff's radiation law, we assume that α_c equals ε_{c}.

$$P_{\mathrm{conv+cond}} = h(T_{\mathrm{amb}} - T_{\mathrm{c}}) \quad \text{(S4)}$$

where h is the thermal transfer coefficient between the ambient and the cooler in the forms of conduction together with convection.

In the calculation for Fig. 1A and Fig. 1B, considering an ideal scenario, the ε_{c}, T_{amb}, h and P_{sun} are assumed to be 1, 25 °C, 0 W m^{-2} K^{-1}, 0 W m^{-2}, respectively. For the calculation in Fig. 1A, T_{c} is set as 30 °C. For the data in Fig. 1B, the $\varepsilon_{\mathrm{amb}}$ is assumed to be 0.724 (*28*).

The cooling power from the evaporative cooling of pure water can be expressed as (*36, 37*)

$$P_{\mathrm{E}} = H_{\mathrm{ev}} \dot{m} \quad \text{(S5)}$$

where, H_{ev} is the enthalpy of water evaporation. $\dot{m}$ denotes the evaporation rate of water.

The enthalpy of pure water evaporation nearly unchangs with water temperature within the range of 30-50 ℃, and is assumed to be 2400 kJ kg^{-1} in the following calculations (*47*).

The water evaporation rate (in a unit of kg m^{-2} h^{-1}) can be expressed as (*48*):

$$\dot{m} = \theta(\chi_S - \chi) \quad \text{(S6)}$$

where, θ is evaporation coefficient, which equals 25 + 19*v*. *v is the* velocity of air above the water surface (unit: m s^{-1}). χ_S denotes the maximum humidity ratio of saturated air at the same temperature as the water surface (kg H_2O in kg dry air). χ is the humidity ratio of ambient air.

Here, we calculate the water evaporation rate under a windless condition (namely, *v* is zero). The ambient temperature and relative humidity are set as 25 ℃ and 40%, respectively. The calculated evaporation rates of pure water (in an open vessel) at different temperatures are shown in fig. S1.

The theoretical cooling power of the TRE cooler is obtained by

$$P_{TRE} = P_R + P_E \quad \text{(S7)}$$

Supplementary Text 2. Optical modeling

The optical scattering of the nanofibers in the solar wavelength range under various diameters was calculated using Mie theory. Here we treat the nanofibers as randomly oriented cylindrical objects, and computed the scattering averaging over both TM and TE polarizations. The refractive index dispersion of cellulose acetate was taken into account in the calculation. It can be observed that having a non-uniform distribution of nanofiber size is important to maintain a strong broadband scattering. The experimentally obtained nanofibers with controllable diameter sizes distributed in the range of 0.5-0.85 um can provide efficient scattering over the major part of the solar spectrum.

Supplementary Figures

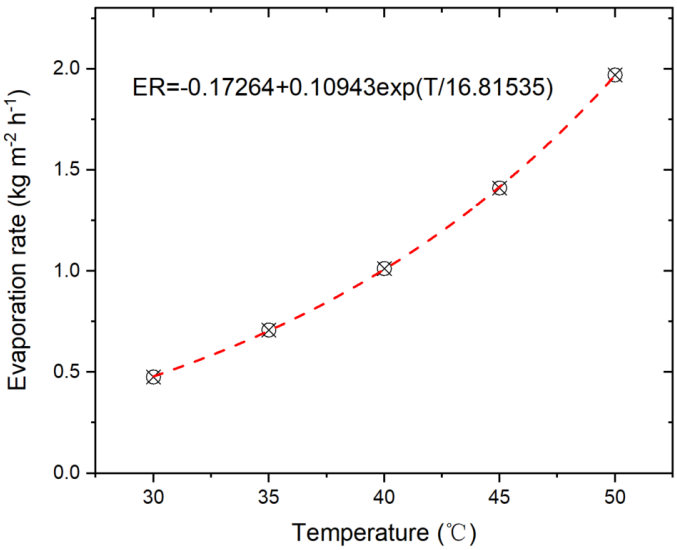

Fig. S1. **Water evaporation rates (abbreviated as *ER*) at different temperatures (shortened to *T*).** The fitting assumes that water evaporation is a tandem process of vaporization coupled with diffusion. Both processes are regarded as first-order kinetic reactions.

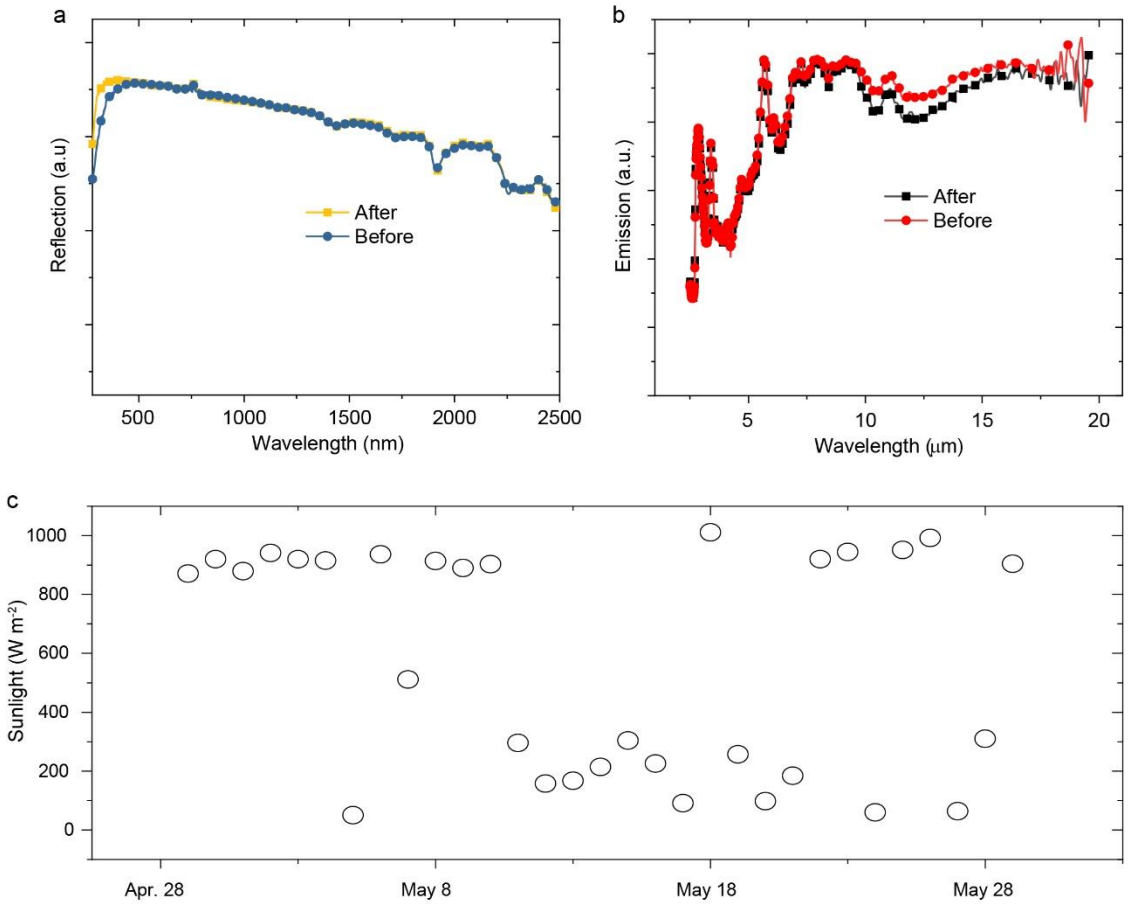

Fig. S2. Stability in optical properties of the CA fibrous network while exposed under outdoor UV light. The solar reflection (**a**) and mid-infrared emission (**b**) spectra of the CA fibrous network before and after 1-month of outdoor exposure. The nearly unchanged optical spectra of the CA fibrous network indicate that it has good UV stability. **c,** Power of midday sunlight during the stability test.

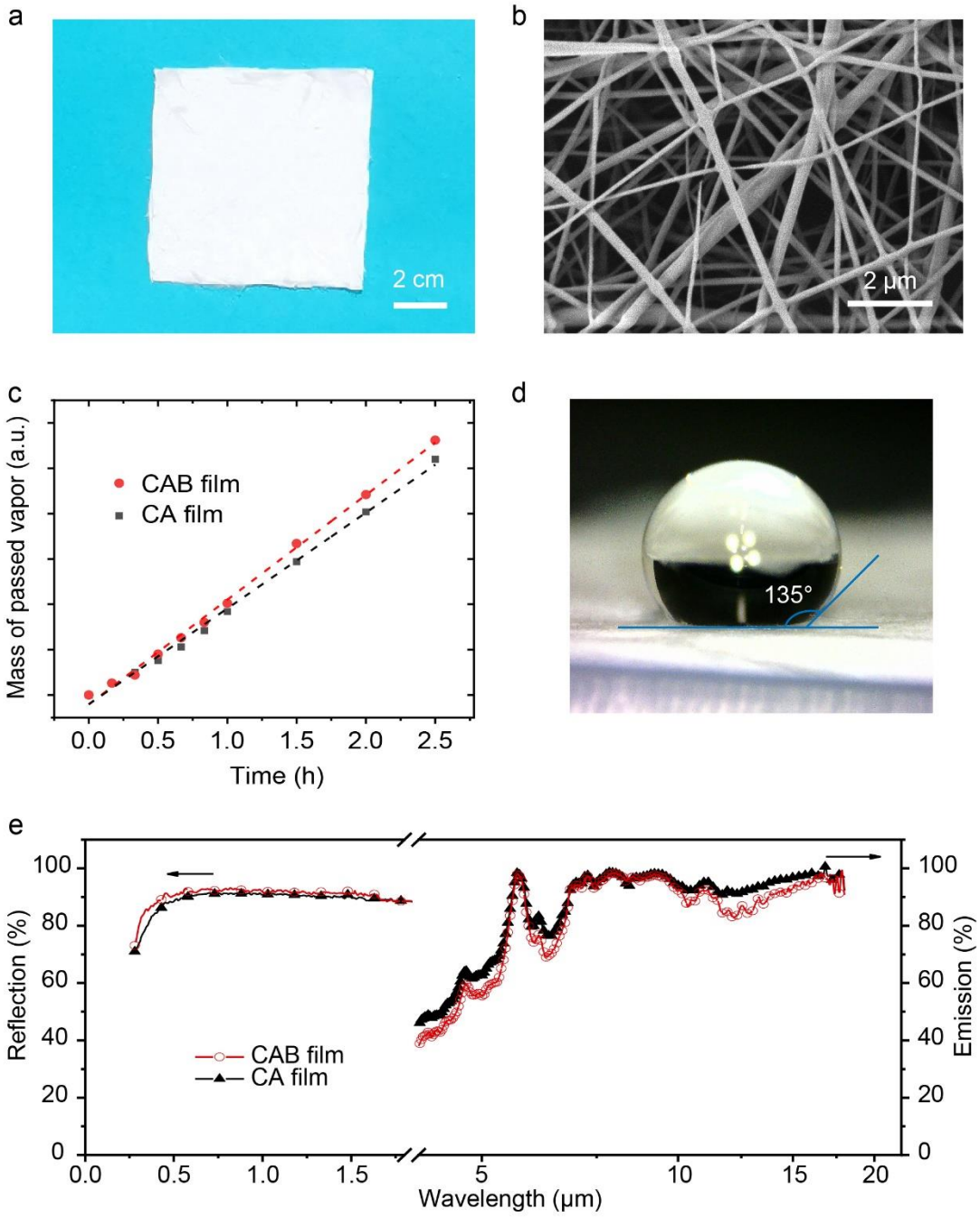

Fig. S3. Characterizations of the cellulose acetate butyrate (abbreviated as CAB) fibrous network and comparisons with the CA fibrous network. CAB is a ramification of CA with recognized UV stability (*49-51*). The CAB fibrous network is also fabricated via electrospinning, with the same solution system of acetone and DMF for the CA fibrous network. **a,** The as-prepared CAB fibrous network appears snow-white like the CA fibrous network. **b,** Nano-fibers randomly stack with each other just as that of the CA fibrous network. **c,** The CAB and CA fibrous networks have similar vapor permeability (slope). **d,** The water contact angle of the CAB fibrous network reaches 135°, resembling that of the CA fibrous network (131°). **e,** The CAB and CA fibrous

networks possess similar sunlight reflection and mid-infrared emission spectra. Photo credit of (a) and (d): Jinlei Li, Nanjing University.

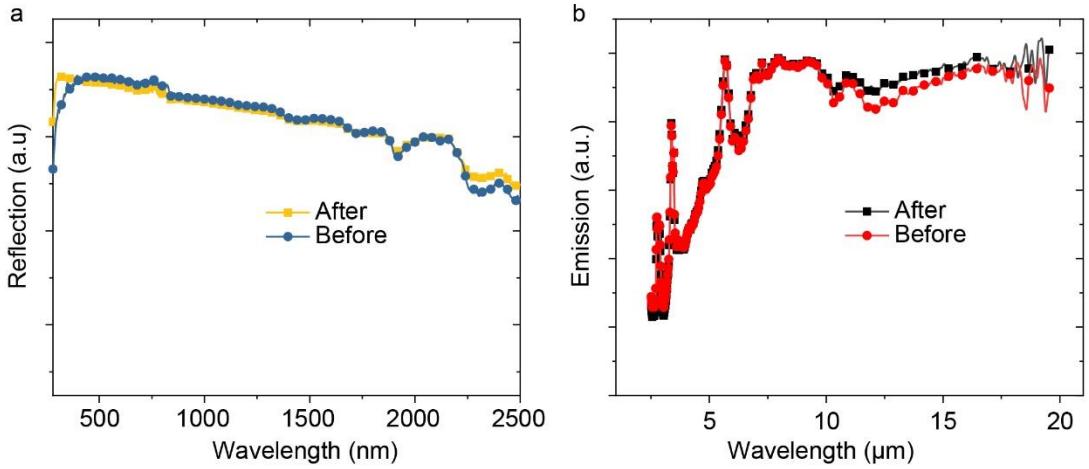

Fig. S4. Stability in optical properties of the CAB fibrous network while exposed under outdoor UV light. The solar reflection (**a**) and mid-infrared emission (**b**) spectra of the CAB fibrous network before and after 1-month of outdoor exposure. The nearly unchanged optical spectra reflect the excellent UV stability of the CAB fibrous network.

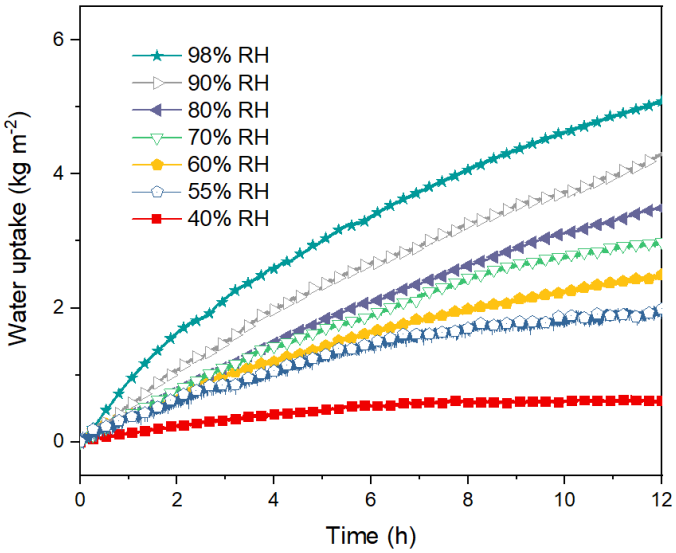

Fig. S5. Moisture adsorption curves of the PVA-$CaCl_2$ hydrogel under different humilities.

The ambient temperature was controlled to be ~25 ℃.

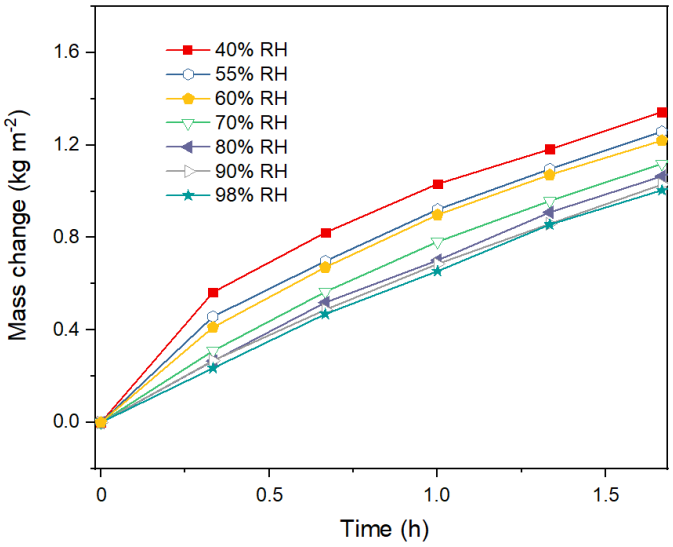

Fig. S6. Evaporation curves of the PVA-$CaCl_2$ hydrogel under different humilities. The ambient temperature and heating temperature were controlled around 25 ℃ and 50 ℃, respectively.

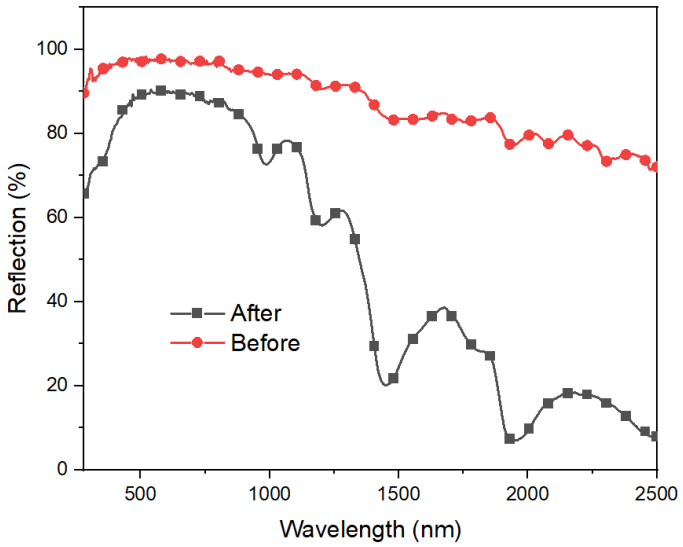

Fig. S7. **Reflection spectra of the PVA-$CaCl_2$ hydrogel before and after moisture adsorption.** The intrinsic optical absorption of water for sunlight, especially at the near-infrared band, results in a significant decline in reflection.

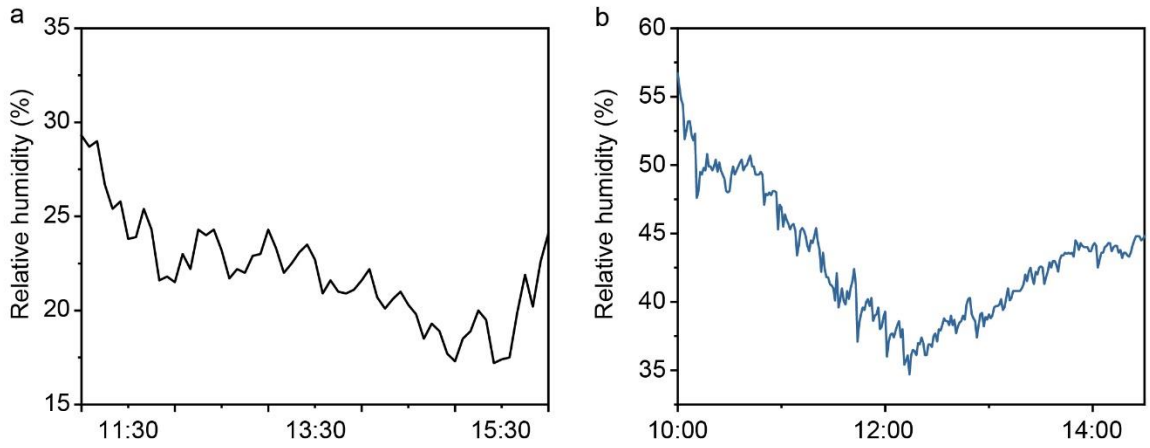

Fig. S8. **Relative humidity of cooling performance measurements in Fig. 3. a** and **b,** Relative humidity of the measurements in Fig. 3D and Fig. 3F, respectively.

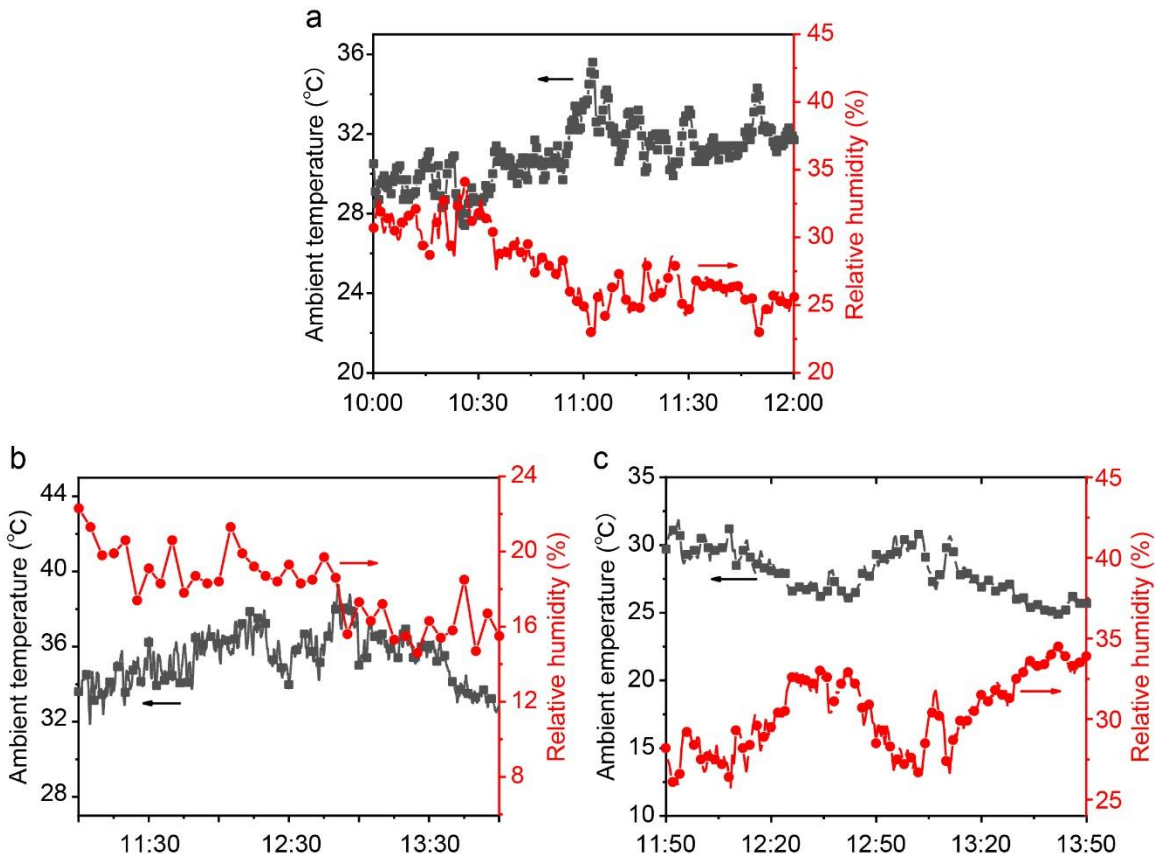

Fig. S9. **Ambient conditions of cooling performance measurements in Fig. 4. a-c,** Ambient conditions of Fig. 4C, Fig. 4E, and Fig. 4G, respectively.

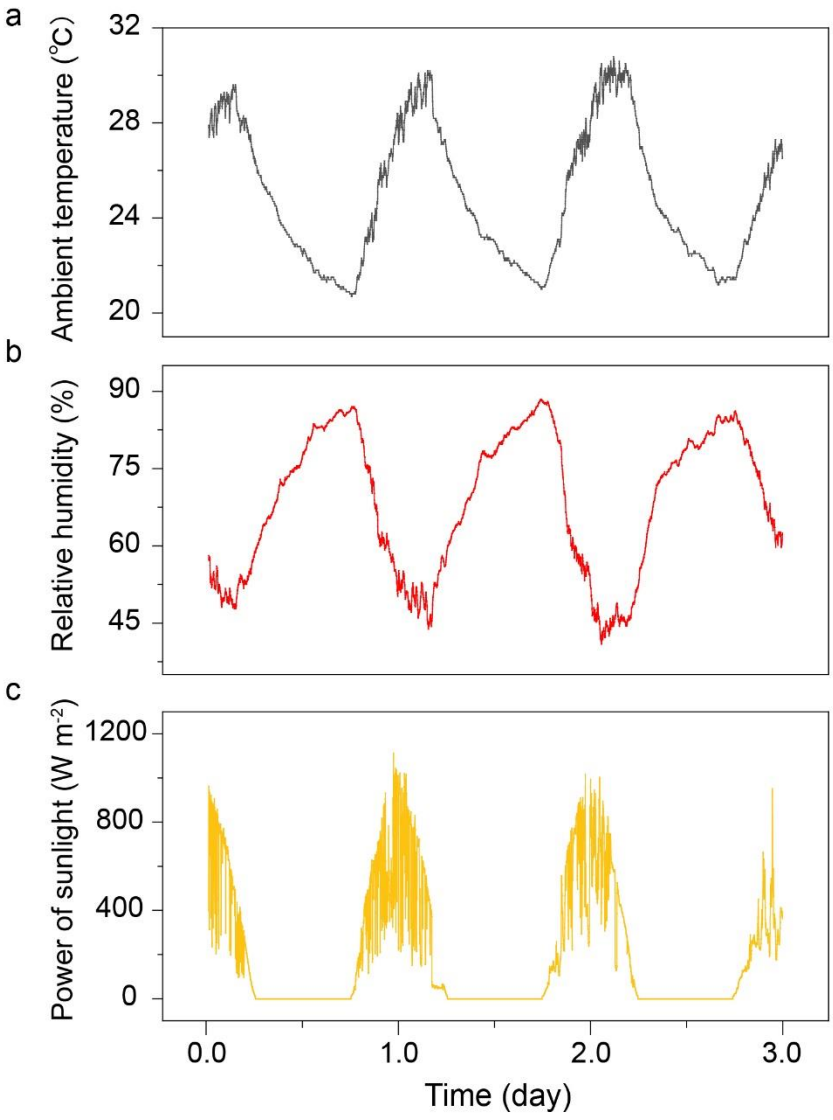

Fig. S10. **Ambient conditions and sunlight power during 3-day continuous cooling measurement in Fig. 4H**. **a-c,** Ambient temperature and relative humidity of air and power of sunlight, respectively.

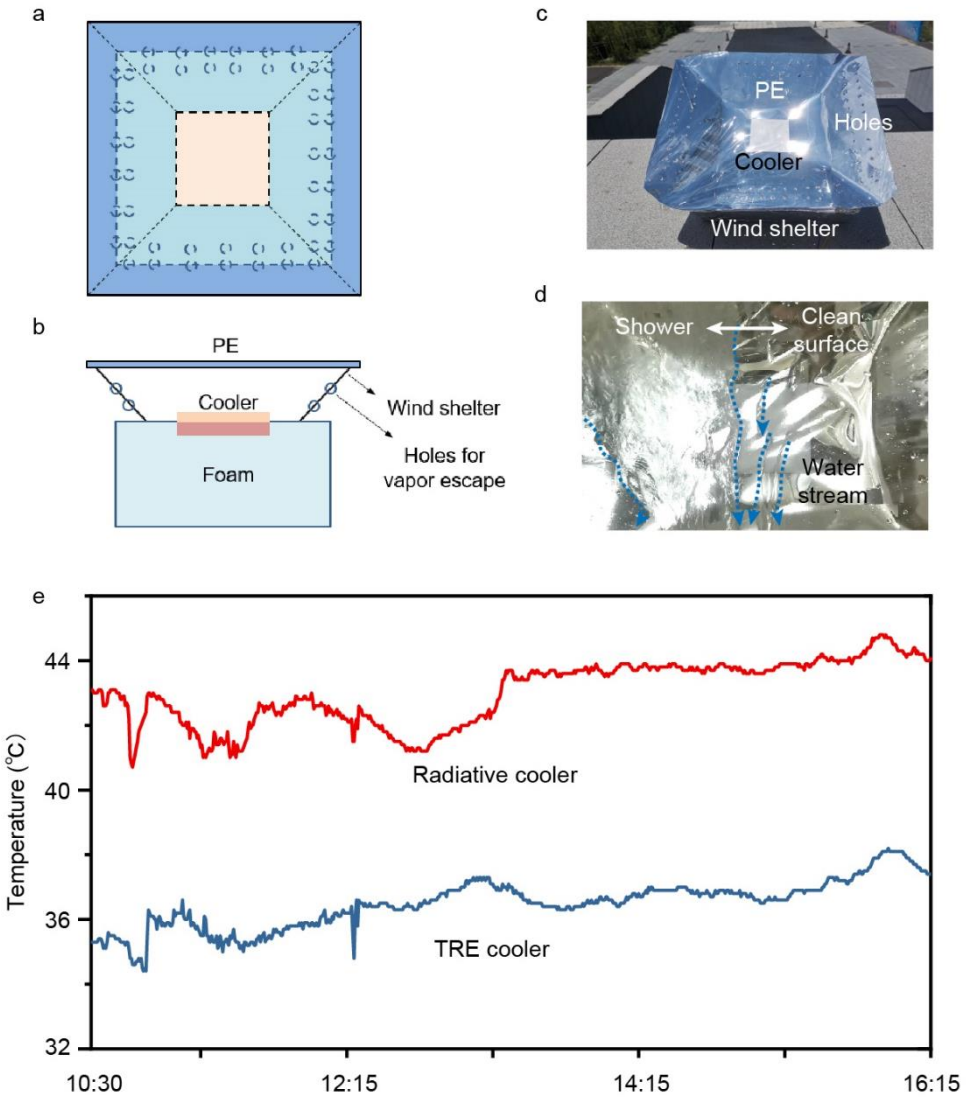

Fig. S11. The experimental setup and cooling performance of the TRE cooler when it rains. a and **b**, Schematics show the bird's view and sectional view of the experimental setup, respectively. The PE film and the groove wind shelter together serve as effective rain shelters. The holes on the wind shelter ensure vapor escape from the TRE cooler to the ambient. **c**, A photograph of the experimental device. **d**, A photograph shows that the PE film is capable of protecting the inner TRE cooler from water/rain. **e**, Temperature comparisons between a TRE cooler and a radiative cooler on a rainy day. A thermal load of ~200 W m^{-2} is applied to the coolers. The TRE cooler is ~6.5 ℃ cooler than the radiative cooler. Photo credit of (c) and (d): Jinlei Li, Nanjing University.

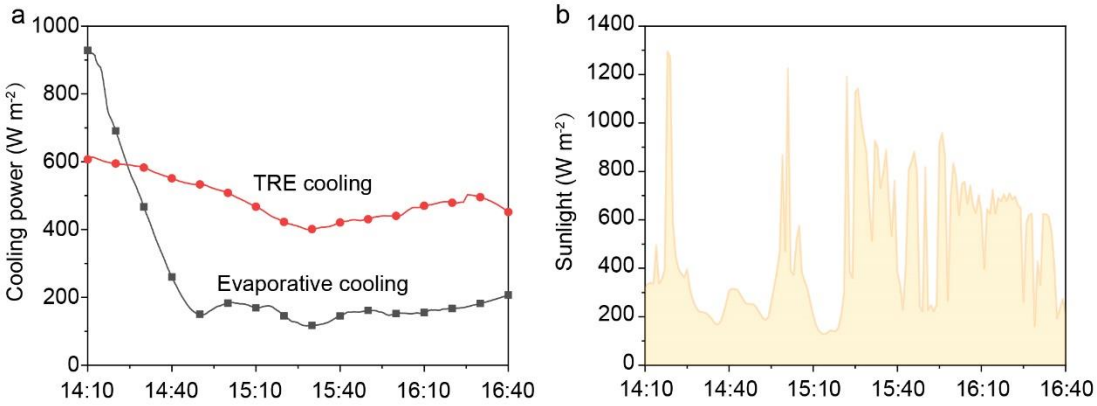

Fig. S12. Comparison of cooling performance between the TRE cooling and conventional evaporative cooling (from a wet white textile) at 50 °C. a, Cooling powers. The cooling capacity, by integrating cooling power with respect to time (namely, the area below the curves of cooling power), of the TRE cooler is much larger than that of the evaporative cooling. This is mainly because the PVA hydrogel is elaborately designed not only to efficiently harvest moisture, but also to have an excellent capacity in storing the captured water to sustain the daytime cooling. **b**, Sunlight power during the cooling power measurement.

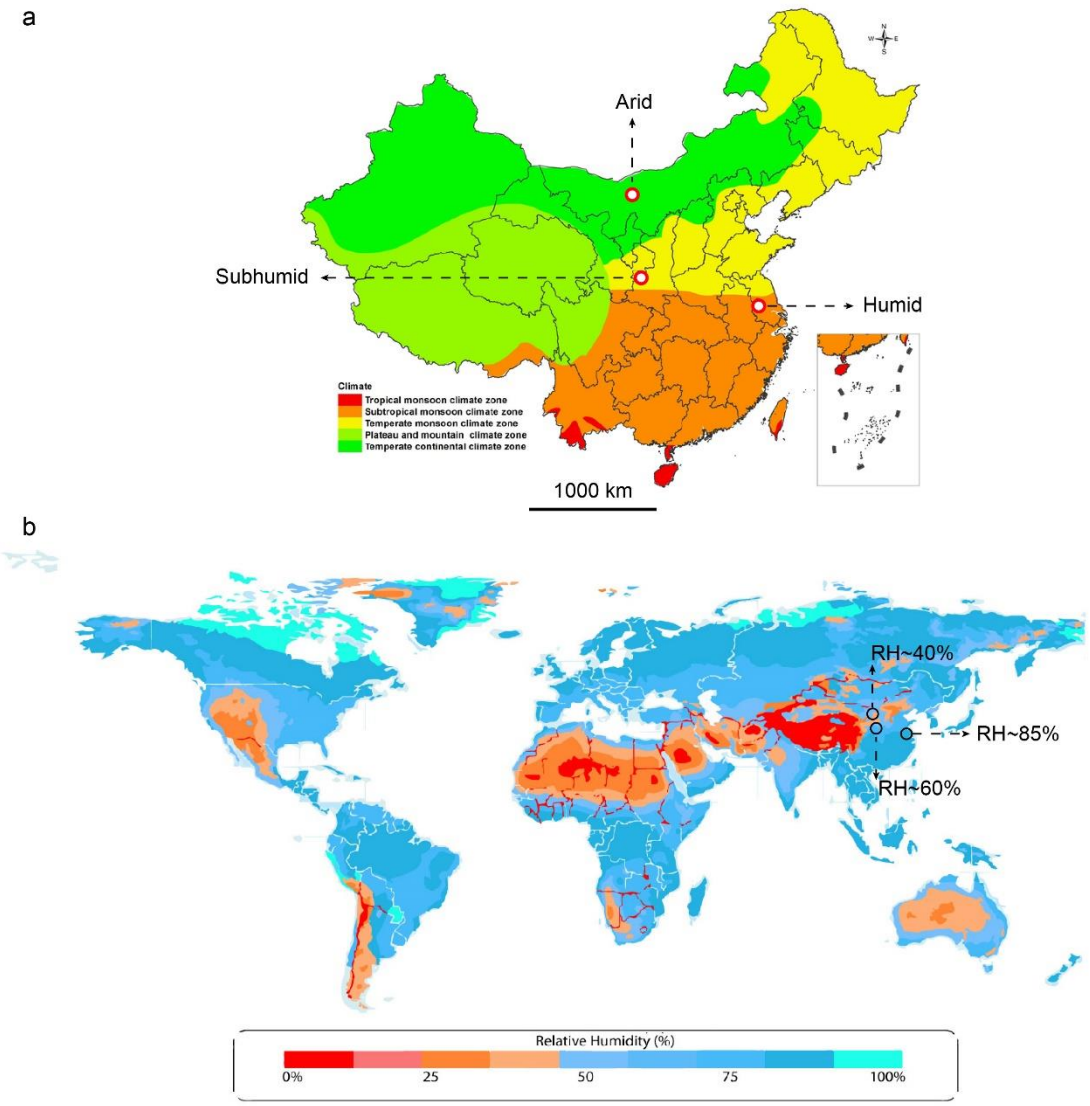

Fig. S13. Climate/humidity map. Maps show the (**a**) climate zone of China and (**b**) global average yearly humidity. The red/black circles denote the places we traveled to measure the cooling performance of the TRE cooler. Our test sites include the three main climate zones of China that require cooling, and the major humidity conditions of the world (accounting for >70% of land surface). Map source: (**a**) PloS one, doi:10.1371/journal.pone.0068102.g003 (*52*), (**b**) University of Wisconsin-madison (*53*).

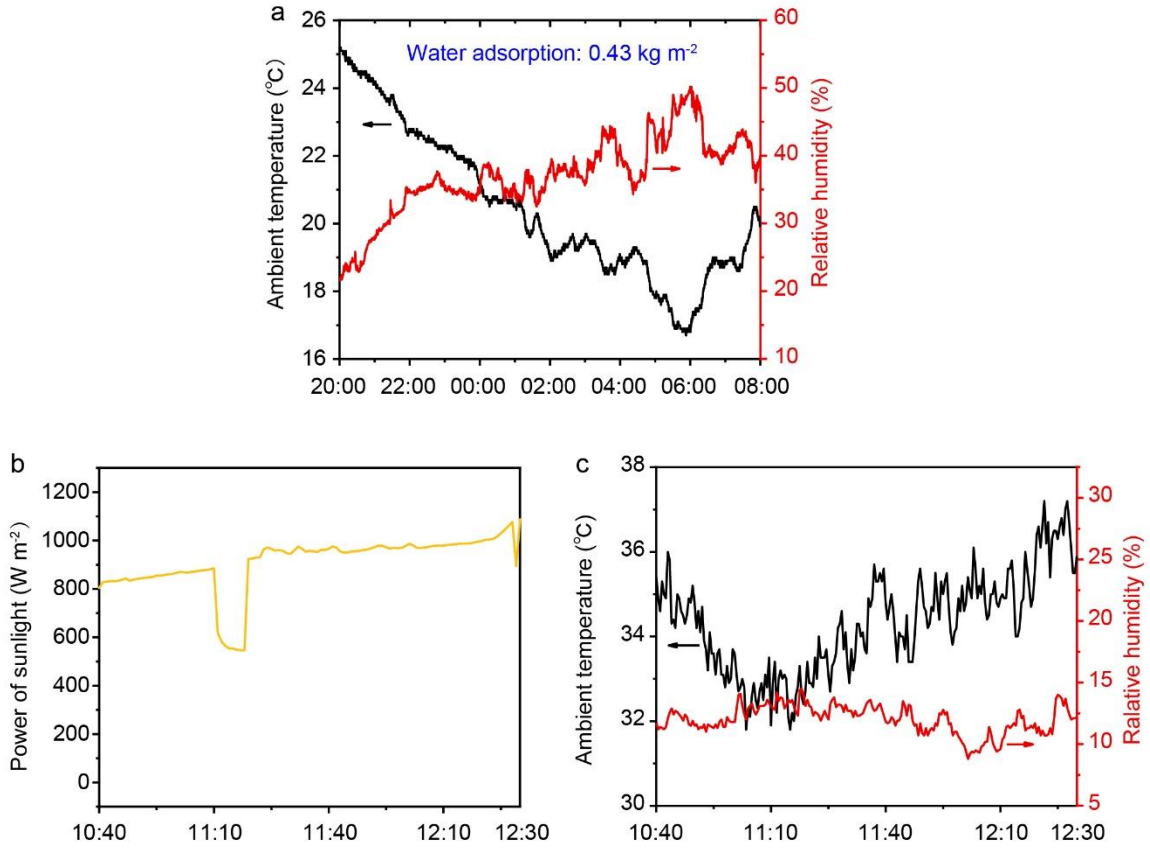

Fig. S14. Ambient conditions of the measurements in the arid climate. a, Ambient temperature and relative humidity during the night. The PVA-$CaCl_2$ hydrogel captures 0.43 kg m^{-2} of water from ambient. **b** and **c,** Sunlight power and ambient temperature together with relative humidity of air during the cooling power measurement in the day, respectively.

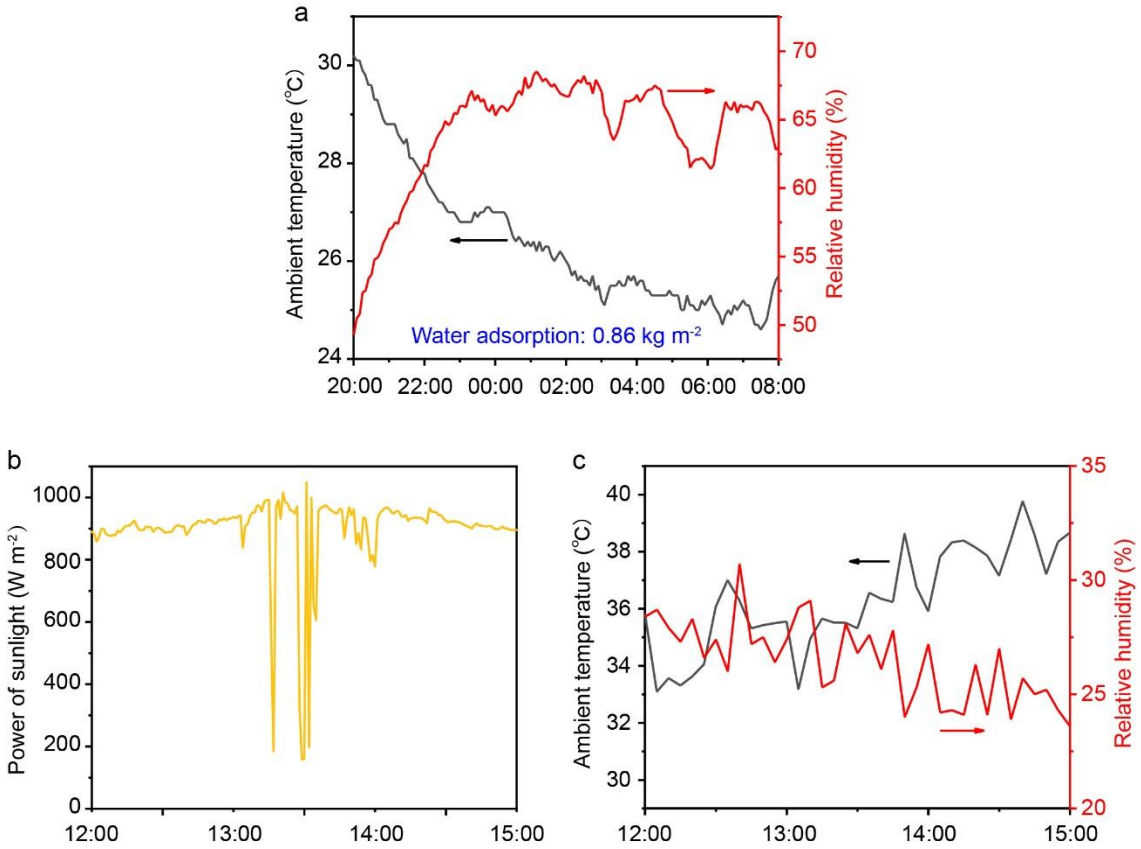

Fig. S15. Ambient conditions of the measurements in the subhumid climate. a, Ambient temperature and relative humidity during the night. The PVA-$CaCl_2$ hydrogel captures 0.86 kg m^{-2} of water from ambient. **b** and **c,** Sunlight power and ambient temperature together with relative humidity of air during the cooling power measurement in the day, respectively.

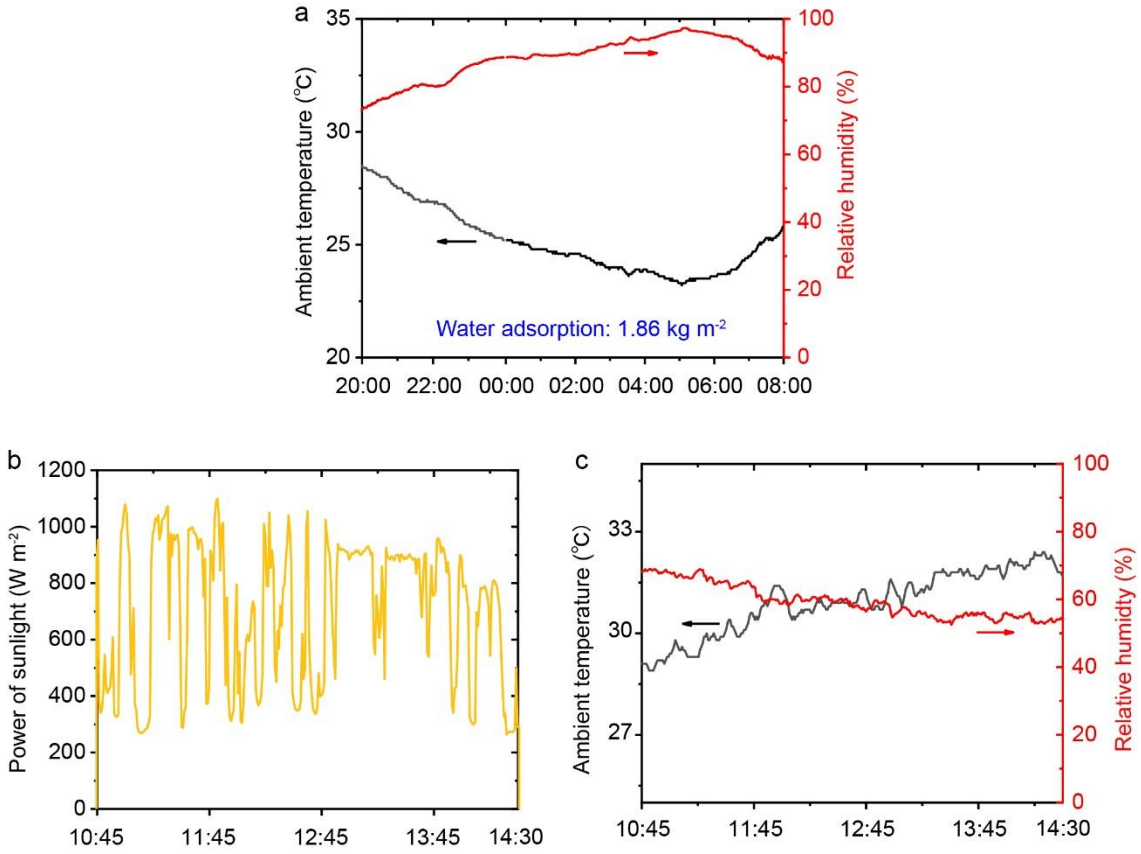

Fig. S16. Ambient conditions of the measurements in the humid climate. a, Ambient temperature and relative humidity during the night. The PVA-$CaCl_2$ hydrogel captures 1.86 kg m^{-2} of water from ambient. **b** and **c,** Sunlight power and ambient temperature together with relative humidity of air during the cooling power measurement in the day, respectively.

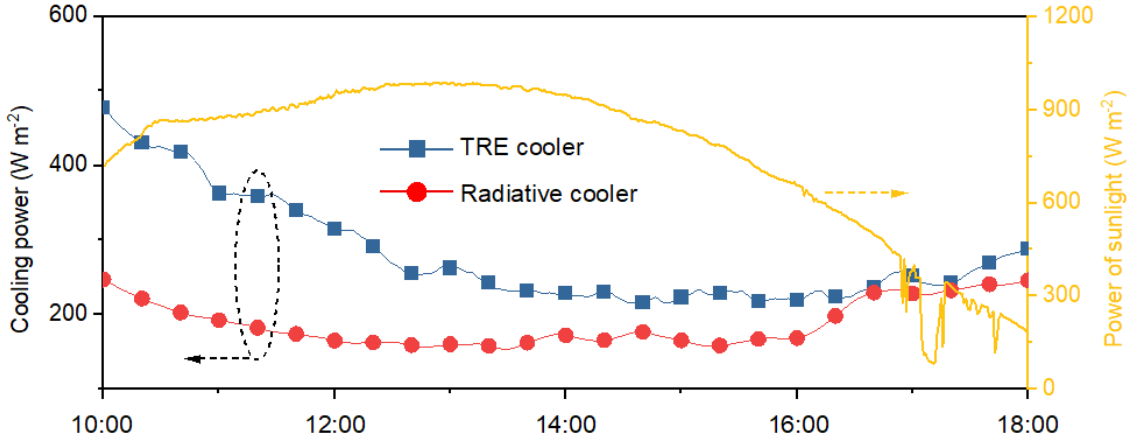

Fig. S17. The cooling powers of the TRE and radiative coolers during the whole day performance test in the subhumid climate. The TRE cooler performs much better cooling compared with the radiative cooler. The yellow line records the sunlight power during the cooling performance test.

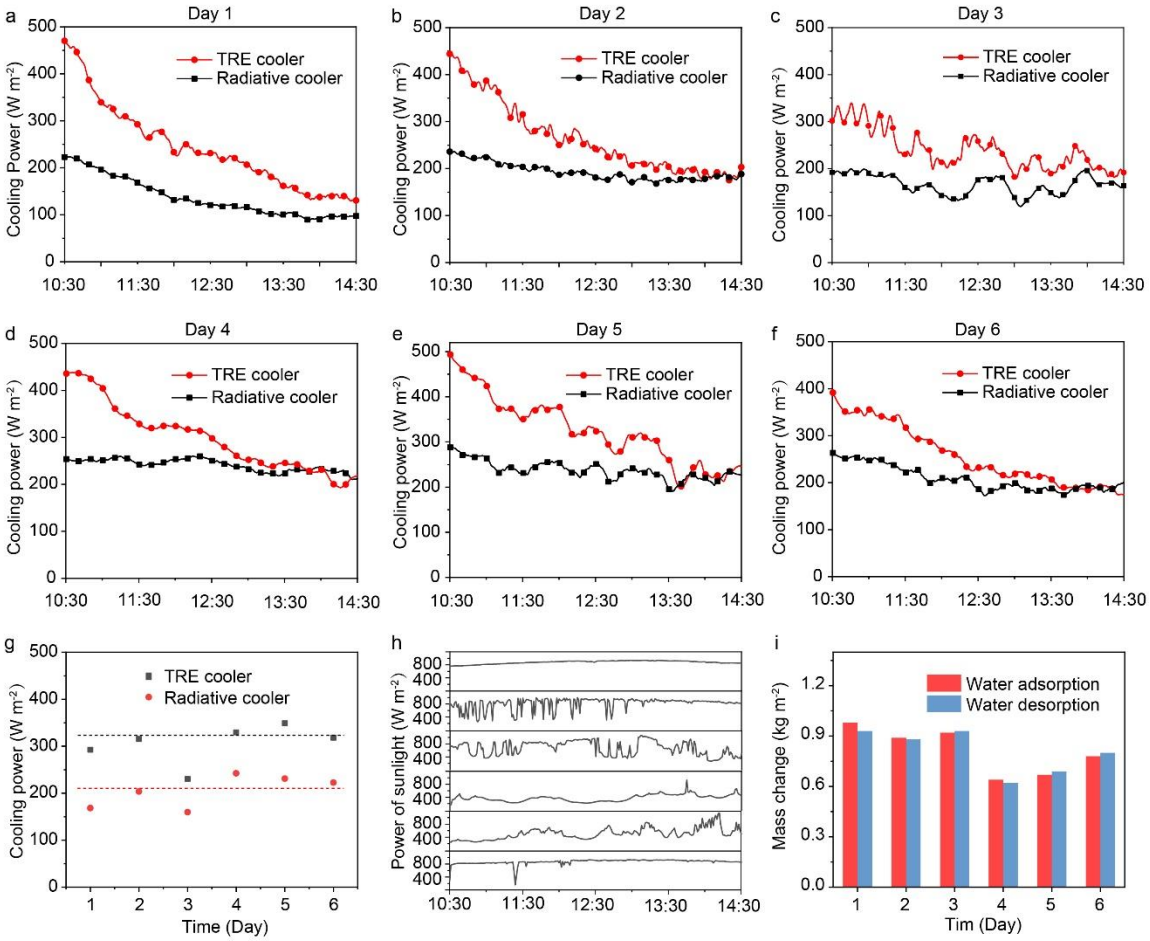

Fig. S18. The continuous cooling power of the TRE cooler in the subhumid climate. a-f, Cooling powers of the TRE and radiative coolers during the 6 days of continuous measurements. The cooling powers of TRE cooler are higher than that of the radiative cooler until the stored water is used up. Then their cooling powers, both from radiative cooling, stay at the same level. The higher cooling performance of the TRE cooler supports better cooling during the hottest period during the daytime compared to the radiative cooler. **g,** Cooling powers at 11:30 every day of the TRE and radiative coolers. The cooling power of the TRE cooler stays stable and is always higher than that realized by the radiative cooler. **h,** From top to bottom are the powers of sunlight during the 6 days of continuous measurements. **i**, Water adsorption and desorption of the PVA-$CaCl_2$ hydrogel during the 6 days of continuous measurements. Water adsorption matches desorption.

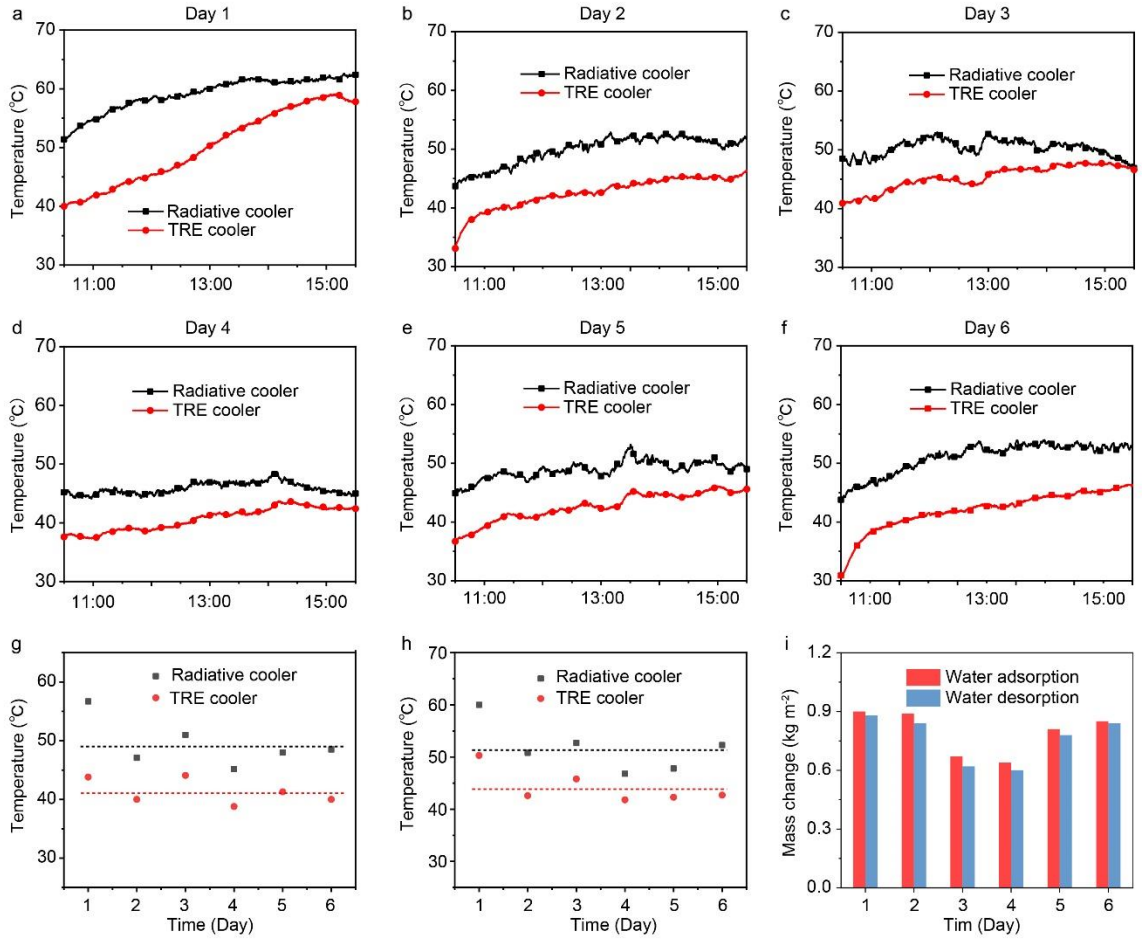

Fig. S19. Continuous temperature measurements of the TRE cooler in the subhumid climate. **a-f,** Temperatures of the TRE and radiative coolers under a heating load of ~ 200 W m^{-2}. 6 days of continuous measurements are presented, respectively. The temperatures of the TRE cooler are always lower than that of the radiative cooler during the hottest 5 hours of daytime, indicating the better cooling performance enabled by the TRE cooler. **g** and **h,** Temperatures of the TRE and radiative coolers at (**g**)11:30 and (**h**)13:00 every day. The temperature of the TRE cooler is stably lower than that of the radiative cooler. **i**, Water adsorption and desorption of the PVA-$CaCl_2$ hydrogel during the 6 days of continuous measurements. Water adsorption and desorption are accordant.

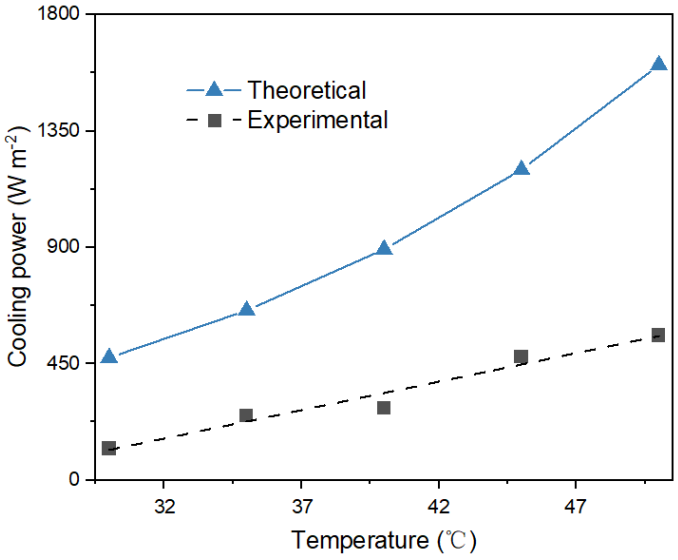

Fig. S20. The realized and expected cooling power of the TRE cooler as a function of working temperatures. Attractive potential in realizing a better cooling performance of the TRE cooler is predicted. In the future, further optimizing the atmospheric moisture harvesting along with water desorption properties (such as minimizing the water evaporation enthalpy (*54*)) and reflectivity/emissivity spectra of the TRE cooler can lead to ongoing improvement in the passive cooling power of the TRE cooler during daytime.

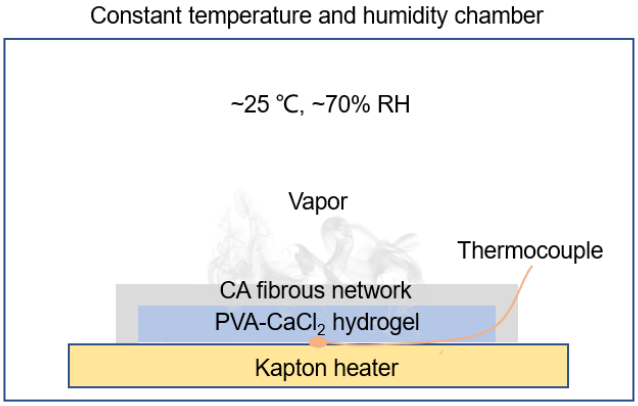

Fig. S21. A schematic of the test device for obtaining the water desorption curves of PVA-$CaCl_2$ hydrogel with/without the CA fibrous network.

Supplementary Table

Table S1. Comparisons in cooling power with literatures. The asterisk (*) denotes the value is estimated according to the information provided in the reference.

Reference	Working temperature (℃)	Cooling power (W m^{-2})
This work	~50	~500 (Fig. 4C)
PAM-CNT hydrogel (*36*)	~50	~331
MIL-101(Cr) powders onto metallic substrate (*37*)	~54	~313*
Li-PAAm hydrogel (*38*)	~50	~112*
rGO/ionogel (RIG) (*55*)	~50	~0.55*
LiBr Hydrogel (*56*)	~50	~157*
Zn-PAAm hydrogel (*57*)	~50	~190*

REFERENCES AND NOTES

1. International Energy Agency, “The future of cooling: Opportunities for energy-efficient air conditioning” (International Energy Agency, 2018); www.iea.org/reports/the-future-of-cooling.

2. A. S. Fleischer, Cooling our insatiable demand for data. *Science* **370**, 783–784 (2020).

3. E. Pennisi, Living with heat. *Science* **370**, 778–781 (2020).

4. M. Santamouris, J. J. B. Feng, Recent progress in daytime radiative cooling: Is it the air conditioner of the future? *Buildings* **8**, 168 (2018).

5. M. O. McLinden, C. J. Seeton, A. Pearson, New refrigerants and system configurations for vapor-compression refrigeration. *Science* **370**, 791–796 (2020).

6. A. Pacak, W. Worek, Review of dew point evaporative cooling technology for air conditioning applications. *Appl. Sci*. **11**, 934 (2021).

7. Y. Yang, G. Cui, C. Q. Lan, Developments in evaporative cooling and enhanced evaporative cooling - A review. *Renew. Sustain. Energy Rev.* **113**, 109230 (2019).

8. American Society of Heating, Refrigerating and Air-conditioning Engineers, "*2016 ASHRAE Handbook---HVAC Systems and Equipment*" (American Society of Heating, Refrigerating and Air-Conditioning Engineers, 2016); http://arco-hvac.ir/wp-content/uploads/2016/11/ASHRAE-Handbook-2016-HVAC-Systems-and-EquipmentIP.pdf.

9. M. M. Mekonnen, A. Y. Hoekstra, Four billion people facing severe water scarcity. *Sci. Adv*. **2**, e1500323 (2016).

10. E. Rephaeli, A. Raman, S. Fan, Ultrabroadband photonic structures to achieve high-performance daytime radiative cooling. *Nano Lett*. **13**, 1457–1461 (2013).

11. Raman, A. P., Anoma, M. A., Zhu, L., Passive radiative cooling below ambient air temperature under direct sunlight. *Nature* **515**, 540–544 (2014).

12. N. N. Shi, C. Tsai, F. Camino, G. D. Bernard, N. Yu, R. Wehner, Keeping cool: Enhanced optical reflection and radiative heat dissipation in Saharan silver ants. *Science* **349**, 298–301 (2015).

13. E. A. Goldstein, A. P. Raman, S. Fan, Sub-ambient non-evaporative fluid cooling with the sky. *Nat. Energy* **2**, 17143 (2017).

14. B. Zhao, M. K. Hu, X. Z. Ao, N. Chen, G. Pei, Radiative cooling: A review of fundamentals, materials, applications, and prospects. *Appl. Energy* **236**, 489–513 (2019).

15. M. Zeyghami, D. Y. Goswami, E. Stefanakos, A review of clear sky radiative cooling developments and applications in renewable power systems and passive building cooling. *Sol. Energy Mater. Sol. Cells.* **178**, 115–128 (2018).

16. Z. Li, Q. Chen, Y. Song, B. Zhu, J. Zhu, Fundamentals, materials, and applications for daytime radiative cooling. *Adv. Mater. Technol.* **5**, 1901007 (2020).

17. X. Yin, R. Yang, G. Tan, S. Fan, Terrestrial radiative cooling: Using the cold universe as a renewable and sustainable energy source. *Science* **370**, 786–791 (2020).

18. Y. Zhai, Y. Ma, S. N. David, D. Zhao, R. Lou, G. Tan, R. Yang, X. Yin, Scalable-manufactured randomized glass-polymer hybrid metamaterial for daytime radiative cooling. *Science* **355**, 1062–1066 (2017).

19. S. Zeng, S. Pian, M. Su, Z. Wang, M. Wu, X. Liu, M. Chen, Y. Xiang, J. Wu, M. Zhang, Q. Cen, Y. Tang, X. Zhou, Z. Huang, R. Wang, A. Tunuhe, X. Sun, Z. Xia, M. Tian, M. Chen, X. Ma, L. Yang, J. Zhou, H. Zhou, Q. Yang, X. Li, Y. Ma, G. Tao. Hierarchical-morphology metafabric for scalable passive daytime radiative cooling. *Science* **373**, 692–696 (2021).

20. T. Li, Y. Zhai, S. He, W. Gan, Z. Wei, M. Heidarinejad, D. Dalgo, R. Mi, X. Zhao, J. Song, J. Dai, C. Chen, A. Aili, A. Vellore, A. Martini, R. Yang, J. Srebric, X. Yin, L. Hu, A radiative cooling structural material. *Science* **364**, 760–763 (2019).

21. J. Mandal, Y. Fu, A. C. Overvig, M. Jia, K. Sun, N. N. Shi, H. Zhou, X. Xiao, N. Yu, Y. Yang, Hierarchically porous polymer coatings for highly efficient passive daytime radiative cooling. *Science* **362**, 315–319 (2018).

22. A. Leroy, B. Bhatia, C. C. Kelsall, A. Castillejo-Cuberos, M. D. C. H., L. Zhao, L. Zhang, A. M. Guzman, E. N. Wang, High-performance subambient radiative cooling enabled by optically selective and thermally insulating polyethylene aerogel. *Sci. Adv.* **5**, eaat9480 (2019).

23. T. Wang, Y. Wu, L. Shi, X. Hu, M. Chen, L. Wu. A structural polymer for highly efficient all-day passive radiative cooling. *Nat. Commun.* **12**, 365 (2021).

24. D. Li, X. Liu, W. Li, Z. Lin, B. Zhu, Z. Li, J. Li, B. Li, S. Fan, J. Xie, J. Zhu, Scalable and hierarchically designed polymer film as a selective thermal emitter for high-performance all-day radiative cooling. *Nat. Nanotechnol.* **16**, 153–158 (2021).

25. L. Zhou, H. Song, J. Liang, M. Singer, M. Zhou, E. Stegenburgs, N. Zhang, C. Xu, T. Ng, Z. Yu, B. Ooi, Q. Gan, A polydimethylsiloxane-coated metal structure for all-day radiative cooling. *Nat. Sustain.* **2**, 718–724 (2019).

26. P. Hsu, A. Y. Song, P. B. Catrysse, C. Liu, Y. Peng, J. Xie, S. Fan, Y. Cui, Radiative human body cooling by nanoporous polyethylene textile. *Science* **353**, 1019–1023 (2016).

27. H. Zhang, K. C. S. Ly, X. Liu, Z. Chen, M. Yan, Z. Wu, X. Wang, Y. Zheng, H. Zhou, T. Fan, Biologically inspired flexible photonic films for efficient passive radiative cooling. *Proc. Natl. Acad. Sci. U.S.A.* **117**, 14657–14666 (2020).

28. D. Zhao, A. Aili, Y. Zhai, S. Xu, G. Tan, X. Yin, R. Yang, Radiative sky cooling: Fundamental principles, materials, and applications. *Appl. Phy. Rev.* **6**, 021306 (2019).

29. R. Naguib, Total cost of ownership for air cooled and water-cooled chiller systems. *ASHRAE J.* **51**, 42–48 (2009).

30. C. Feng, P. Yang, H. Liu, M. Mao, Y. Liu, T. Xu, J. Fu, T. Cheng, X. Hu, H. Jin Fan, K. Liu, Bilayer porous polymer for efficient passive building cooling. *Nano Energy* **85**, 105971 (2021).

31. Y. Sun, Y. Ji, M. Javed, X. Li, Z. Fan, Y. Wang, Z. Cai, Bi Xu, Preparation of passive daytime cooling fabric with the synergistic effect of radiative cooling and evaporative cooling. *Adv. Mater. Technol.* **7**, 2100803 (2021)

32. Z. Xia, L. Li, K. Shi, Z. Fang, X. Fan, Using passive evaporation to improve radiative cooling performance. *J. Photonics Energy* **12**, 012113 (2021).

33. T. A. Cooper, S. H. Zandavi, G. W. Ni, Y. Tsurimaki, Y. Huang, S. V. Boriskina, G. Chen, Contactless steam generation and superheating under one sun illumination. *Nat. Commun.* **9**, 5086 (2018).

34. G. M. Hale, M. R. Querry, Optical constants of water in the 200-nm to 200-μm wavelength region. *Appl. Optics* **12**, 555–563 (1973).

35. A. C. C. Rotzetter, C. M. Schumacher, S. B. Bubenhofer, R. N. Grass, L. C. Gerber, M. Zeltner,W. J. Stark. Thermoresponsive polymer induced sweating surfaces as an efficient way to passively cool buildings. *Adv. Mater.* **24**, 5352–5356 (2012).

36. R. Li, Y. Shi, M. Wu, S. Hong P. Wang, Photovoltaic panel cooling by atmospheric water sorption-evaporation cycle. *Nat. Sustain.* **3**, 636–643 (2020).

37. C. Wang, L. Hua, H. Yan, B. Li, Y. Tu, R. Wang, A thermal management strategy for electronic devices based on moisture sorption-desorption processes. *Joule* **4**, 435–447 (2020).

38. S. Pu, J. Fu, Y. Liao, L. Ge, Y. Zhou, S. Zhang, S. Zhao, X. Liu, X. Hu, K. Liu, J. Chen, Promoting energy efficiency via a self-adaptive evaporative cooling hydrogel. *Adv. Mater.* **32**, e1907307 (2020).

39. L. Persano, A. Camposeo, C. Tekmen, D. Pisignano, Industrial upscaling of electrospinning and applications of polymer nanofibers: A review. *Macromol. Mater. Eng.* **298**, 504–520 (2013).

40. A. I. Liapis, R. Bruttini, *Handbook of Industrial Drying* (CRC Press, 2020).

41. M. Ejeian, R. Z. Wang, Adsorption-based atmospheric water harvesting. *Joule* **5**, 1678–1703 (2021).

42. F. Fathieh, M. J. Kalmutzki, E. A. Kapustin, P. J. Waller, J. Yang, O. M. Yaghi, Practical water production from desert air. *Sci. Adv.* **4**, eaat3198 (2018).

43. H. Kim, S. R. Rao, E. A. Kapustin, L. Zhao, S. Yang, O. M. Yaghi, E. N. Wang. Adsorption-based atmospheric water harvesting device for arid climates. *Nat. Commun.* **9**, 1191 (2018).

44. J. Sun, X. Zhao, W. R. K. Illeperuma, O. Chaudhuri, K. H. Oh, D. J. Mooney, J. J. Vlassak, Z. Suo, Highly stretchable and tough hydrogels. *Nature* **489**, 133–136 (2012).

45. M. Hua, S. Wu, Y. Ma, Y. Zhao, Z. Chen, I. Frenkel, J. Strzalka, H. Zhou, X. Zhu, X. He, Strong tough hydrogels via the synergy of freeze-casting and salting out. *Nature* **590**, 594–599 (2021).

46. W. Li, S. Fan, Radiative cooling: Harvesting the coldness of the universe. *Opt. Photonics News* **30**, 32–39 (2019).

47 "Water-Heat of Vaporization" (Engineering ToolBox); *www.engineeringtoolbox.com/water-properties-d_1573.html*

48. "Evaporation from Water Surface" (Engineering ToolBox); *www.engineeringtoolbox.com/evaporation-water-surface-d_690.html*

49. J. E. Ayuk, A. P. Mathew, K. Oksman, The effect of plasticizer and cellulose nanowhisker content on the dispersion and properties of cellulose acetate butyrate nanocomposites. *J. Appl. Polym. Sci.* **114**, 2723–2730 (2009).

50. R. M. Raouf, Z. A. Wahab, N. A. Ibrahim, Z. A. Talib, B. W. Chieng, Transparent blend of poly (methylmethacrylate)/cellulose acetate butyrate for the protection from ultraviolet. *Polymers* **8**, 128 (2016).

51. R. Hu, B. Huang, Z. Xue, Q. Li, T. Xia, W. Zhang, C. Lu, H. Xu, Synthesis of photocurable cellulose acetate butyrate resin for continuous liquid interface production of three-dimensional objects with excellent mechanical and chemical-resistant properties. *Carbohydr. Polym.* **207**, 609–618 (2019).

52. X. Li, L. Wang, H. Zhang, X. Du, S. Jiang, T. Shen, Y. Zhang, G. Zeng, Seasonal variations in notification of active tuberculosis cases in China, 2005–2012. *PLOS ONE* **8**, e68102 (2013).

53. "Average yearly humidity" (University of Wisconsin-madison); https://digitalfilmmaker.net/ruggard-dry-cabinet-dehumidifier/.

54. F. Zhao, X. Zhou, Y. Shi, X. Qian, M. Alexander, X. Zhao, S. Mendez, R. Yang, L. Qu, G. Yu, Highly efficient solar vapour generation via hierarchically nanostructured gels. *Nat. Nanotech.* **13**, 489–495 (2018).

55. F. Ni, P. Xiao, C. Zhang, W. Zhou, D. Liu, S. Kuo, T. Chen, Atmospheric hygroscopic ionogels with dynamically stable cooling interfaces enable a durable thermoelectric performance enhancement. *Adv. Mater.* **33**, 2103937 (2021).

56. S. Pu, Y. Liao, K. Chen, J. Fu, S. Zhang, L. Ge, G. Conta, S. Bouzarif, T. Cheng, X. Hu, K. Liu, J. Chen, Thermogalvanic hydrogel for synchronous evaporative cooling and low-grade heat energy harvesting. *Nano Lett.* **20**, 3791–3797 (2020).

57. P. Yang, C. Feng, Y. Liu, T. Cheng, X. Yang, H. Liu, K. Liu, H. Fan, Thermal self-protection of zinc-ion batteries enabled by smart hygroscopic hydrogel electrolytes. *Adv. Energy Mater.* **10**, 2002898 (2020).